

Enhancing performance of magnetized liner inertial fusion at the Z facility

S. A. Slutz, M. R. Gomez, S. B. Hansen, E. C. Harding, B. T. Hutzel, P. F. Knapp, D. C. Lamppa, T. J. Awe, D. J. Ampleford, D. E. Bliss, G. A. Chandler, M. E. Cuneo, M. Geissel, M. E. Glinsky, A. J. Harvey-Thompson, M. H. Hess, C. A. Jennings, B. Jones, G. R. Laity, M. R. Martin, K. J. Peterson, J. L. Porter, P. K. Rambo, G. A. Rochau, C. L. Ruiz, M. E. Savage, J. Schwarz, P. F. Schmit, G. Shipley, D. B. Sinars, I. C. Smith, R. A. Vesey, and M. R. Weis

Sandia National Laboratories, Albuquerque, New Mexico 87185, USA

(Received 30 August 2018; accepted 10 October 2018; published online 21 November 2018)

The Magnetized Liner Inertial Fusion concept (MagLIF) [Slutz *et al.*, Phys. Plasmas **17**, 056303 (2010)] is being studied on the Z facility at Sandia National Laboratories. Neutron yields greater than 10^{12} have been achieved with a drive current in the range of 17–18 MA and pure deuterium fuel [Gomez *et al.*, Phys. Rev. Lett. **113**, 155003 (2014)]. We show that 2D simulated yields are about twice the best yields obtained on Z and that a likely cause of this difference is the mix of material into the fuel. Mitigation strategies are presented. Previous numerical studies indicate that much larger yields (10–1000 MJ) should be possible with pulsed power machines producing larger drive currents (45–60 MA) than can be produced by the Z machine [Slutz *et al.*, Phys. Plasmas **23**, 022702 (2016)]. To test the accuracy of these 2D simulations, we present modifications to MagLIF experiments using the existing Z facility, for which 2D simulations predict a 100-fold enhancement of MagLIF fusion yields and considerable increases in burn temperatures. Experimental verification of these predictions would increase the credibility of predictions at higher drive currents. *Published by AIP Publishing.* <https://doi.org/10.1063/1.5054317>

I. INTRODUCTION

The conventional laser approach¹ to inertial confinement fusion (ICF) is to heat the outside surface of a spherical capsule to generate high ablation pressures (>100 Mbars) and implosion velocities (~ 400 km/s) by either direct laser heating or indirect heating with x-rays. Pulsed power offers the much more efficient approach of using magnetic pressure to directly drive cylindrical implosions but only to velocities of 70–150 km/s when the liner thickness is sufficient to eliminate feedthrough of hydrodynamic instabilities. The high temperatures needed for fusion can still be obtained with Magneto-Inertial Fusion (MIF) concepts where the fuel is magnetized to limit conduction losses and preheated before the implosion so that very high convergence is not required. In addition, the initial magnetic field is increased by flux compression during the implosion to strengths sufficient to confine the fusion products.^{2,3}

Magnetized Liner Inertial Fusion (MagLIF)^{4–6} is a specific MIF concept, which is being studied at the Z facility. The fuel (deuterium or deuterium/tritium) is contained in a metal tube called a liner, which is magnetized by external field coils [see Fig. 1(a)]. The liner must be long enough so that axial transport losses are acceptable without closed field lines. A 1 cm length is sufficient for implosions driven by the Z machine, with a current rise-time of 100 ns. The drive current flows axially along the outer surface of the liner and generates an azimuthal magnetic field in addition to the initial axial field. This azimuthal field provides pressure that drives the liner inward radially. The Z Beamlet laser,⁷ which preheats the fuel to an average temperature in the range of 100–200 eV, is fired when the liner starts to move inward.

Cushions [see Fig. 1(b)] are provided inside the liner at each end to mitigate the “wall instability,” which occurs at the boundary between a z-pinch liner and the wall (slide surface).

The axial magnetic field is frozen into the fuel due to the high conductivity after preheat. Thus, as the liner is compressed, the magnetic field rises to very high values ($\sim 10^4$ T), which strongly inhibits radial electron thermal conduction loss near stagnation when the losses would be the greatest due to the high fuel temperatures.

Numerical simulations and experiments^{4,8–12} indicate that thick walled liners with an aspect ratio ($A_R = R_{\text{outer}}/\Delta R_{\text{wall}} \sim 6$) should be robust to the Rayleigh Taylor (RT) instability, which would break up thin-walled liner implosions. Larger aspect ratios may be possible with the suppression of the electro-thermal instability,^{13,14} but we use the conservative value $A_R = 6$ for this study.

Numerous experiments have been performed on the Z accelerator,^{15,16} which validate the basic physics underlying the MagLIF concept. The primary deuterium-deuterium (DD) neutron yield is measured using indium activation^{17–20} samples located at three azimuthal positions at three polar angles. A simplified MCNP (Monte Carlo N-particle)²¹ model of the load region is used to estimate the expected activation as a function of neutron yield. The uncertainty in the measurement is approximately 20% and is dominated by the scattering environment. Typically, the variation in the yield inferred from each of the activation samples is much less than the uncertainty in the measurement.

Neutron yields of up to 5×10^{12} have been measured²² on MagLIF experiments. Deuterium plasma temperatures up

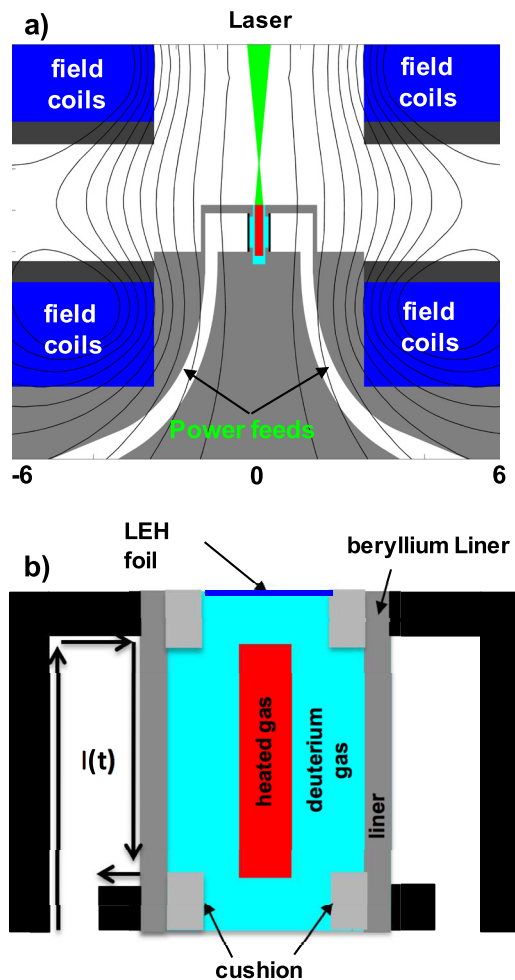


FIG. 1. The MagLIF geometry: (a) zoomed out to include field coils and (b) zoomed in for smaller details.

to 3.0 keV have been determined by both neutron time of flight (NTOF)^{20,23} and x-ray spectroscopy.²⁴ In addition, secondary deuterium-tritium (DT) neutrons have been measured, indicating a high degree of magnetization.²⁵ So far, most of the experiments have been limited to low fuel preheat energy (<1 kJ), low fuel density (0.7 kg/m³), modest axial field (10 T), and low drive current (<18 MA), which have limited the performance.

Z Beamlet was originally a prototype for the NIF laser. It is a frequency doubled (0.53 μm) neodymium glass laser that was moved to the Z facility to provide x-rays for backlighting⁷ for which beam smoothing is not required. The initial MagLIF experiments were performed with a 1 TW unsmoothed beam, which had large intensity variations that drove laser plasma instabilities (LPI). A polyimide foil is used to contain the deuterium at the laser entrance hole (LEH). Laser-only experiments²⁶ using Z Beamlet indicated that only about 10% of the approximate 2 kJ of laser energy penetrates a 3.5 μm foil that was used in the early experiments, which had yielded $1\text{--}2 \times 10^{12}$ neutrons. Later experiments were performed with thinner foil (~ 1.8 μm) and increased yields, $2\text{--}5 \times 10^{12}$. An experiment was performed with an increased laser energy of about 4 kJ and a 1.8 μm foil, which did not show improved yield although the laser energy entering the fuel should have been increased. The

leading hypothesis was that the unsmoothed beam filaments sprays outward, striking the target cushion and inducing mix into the fuel. The benefit of increased preheat could thus easily be canceled by an increase in mix. We present simulations, indicating that if mix can be mitigated, the present yields could be significantly improved by increasing the preheat but only if the initial magnetic field strength and fuel density are also increased.

More recently, experiments using the 0.35 μm Omega-EP (Extended Performance) laser^{27,28} and the Z Beamlet laser²⁹ have demonstrated 40% energy coupling into the fuel by using phase plate smoothing and lower laser power (0.5 TW). Yields of 4×10^{12} have been obtained with this approach, which delivered about 0.8 kJ to the fuel. We would like to increase the preheat energy, but the Z Beamlet pulse is presently limited to 2 kJ at the lower powers (longer pulse length) due to plasma closure of a spatial filter. The spatial filter will be modified soon to allow increased preheat and consequently higher fuel densities. Even for a low-power smoothed beam, a large fraction of the beam is absorbed in the LEH foil. We will describe methods to either use a very thin foil or remove it entirely before the preheat laser pulse arrives.

Simulations indicate that increased axial magnetic field strength is needed to significantly improve the performance. However, maintaining x-ray diagnostic access has limited the available coils to only allow marginal increases in magnetic field strength above 10 T provided for most MagLIF experiments. Coils capable of generating fields greater than 20 T are under development and will be tested soon. The existing coil sets affect the power feed as can be seen in Fig. 1(a), where the power feed must travel a significant distance vertically as it passes through the lower field coil set. This adds inductance to the feed, which adversely affects the maximum current that the Z machine can deliver. The existing MagLIF feed and load geometry (inside the post-hole convolute) have an inductance of 7.2 nH, which limits the peak current to less than 18 MA. We will present alternatives to the existing field coil design and power feed which could produce higher magnetic fields with lower feed inductance, thus increasing the drive current.

2D LASNEX simulations³⁰ indicate that MagLIF could produce high yields on future pulsed power machines,³¹ but although these are detailed simulations, important physics could be missing. We present a path that according to simulations should increase MagLIF yields 100-fold on the existing machine. These MagLIF experiments will be performed over the next several years to test these simulation predictions and refine our models if necessary. The uncertainty in projecting MagLIF performance to future pulsed power facilities will be significantly reduced when simulations can describe MagLIF performance over the large performance space available with the Z machine.

II. NUMERICAL MODEL OF MagLIF IMPLOSIONS

The code LASNEX³² was used for all simulations reported in this study. LASNEX solves the resistive magneto-hydrodynamics equations and includes radiation transport, the effect of magnetic fields on thermal

conductivity, and the transport of fusion generated particles, e.g., α -particles. The LASNEX simulations include a circuit model to self-consistently calculate the drive current from the Z-accelerator. LASNEX includes non-ideal Magneto-Hydrodynamic (MHD) terms due to the Hall and Nernst effects, which are important to MagLIF operation⁴ and detailed models of the equation of state and the electrical resistivity for the fusion fuel (DT) and liner material (Beryllium). The simulations were started at room temperature with the effects of joule heating on melting and vaporization of the liner material included.

Inevitably, some of the liner material will be mixed into the fuel during the implosion, which will enhance radiation losses. A low-atomic number material is thus desirable because radiation losses increase with the atomic number. Furthermore, the implosion velocity of thick ($A_R = 6$) liners is higher for a low-density material. Beryllium has been used for all MagLIF experiments to date because it is the most convenient low-atomic number low-density material. Lithium is another possible candidate but less convenient due to its chemical reactivity. Other possibilities include composite liners with tailored density profiles to reduce the effects of the RT instability and frozen deuterium or DT liners to remove the enhancement of radiation losses due to mix. For simplicity, we assume beryllium liners with $A_R = 6$ for this study.

The geometry of the 2D simulations shown in Fig. 1(b) is the same as for a previous study of MagLIF performance on future machines.³⁰ A uniform axial magnetic field is applied over the entire volume of the simulation. The liner is shown as dark gray, and the liner cushions placed inside the liner at both ends to define the length of the imploding region are shown as light gray. The gaseous deuterium (or deuterium/tritium) fuel is shown in cyan. A vacuum region (not shown) is provided above and below the laser entrance holes. This allows some fuel to escape during the implosion, which is a process not captured by 1D simulations. In this study, we do not simulate laser deposition within the fuel but simply deliver this energy at a fixed power (typically 0.5–1 TW) to the region shown in red. This is the most desirable region to preheat since gas within the cushions will not be imploded by the liner. This form of preheat will be possible using the laser-gate concept that we will present later in this paper. The heated region has a diameter of 1.2 mm, which is substantially smaller than the inner diameter of the liner (4.6 mm). Consequently, the heated gas generates a blast wave which propagates in the positive radial direction. The timing of the preheat is adjusted so that the outward propagating blast wave and the inward traveling shock wave from the current drive reach the inner boundary of the liner at the same time. This should minimize spall from this inside surface of the liner. The path of the drive current is indicated in Fig. 1(b).

The magnitude of the current is found by solving the circuit illustrated in Fig. 2(a). The voltage source, V_S , is the effective time-dependent open circuit voltage of the Z machine, which rises to about 7 MV in 100 ns. This voltage is proportional to the initial charge voltage of the Marx generators. The effective impedance of the accelerator is

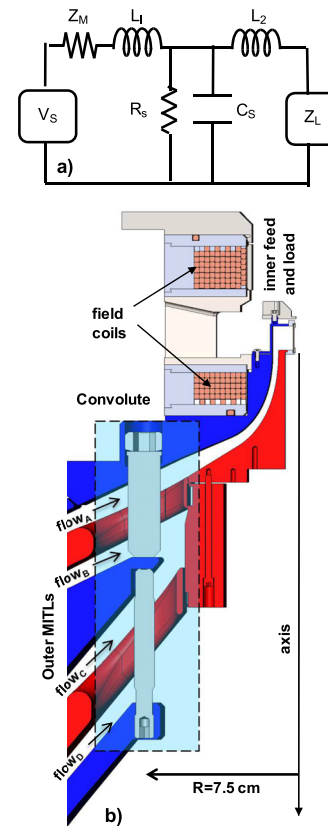


FIG. 2. (a) Equivalent circuit for pulsed power accelerators driving a MagLIF load. (b) Schematic of the post-hole convolute used to add current from each of the transmission line levels (a-d) and the inner feed that drives the MagLIF load.

$Z_M = 0.18 \Omega$, while the time-dependent impedance of the load Z_L is determined self-consistently by the simulations. The present Z accelerator feeds current from the water section into four levels of magnetically insulated vacuum transmission lines (MITLs) [see Fig. 2(b)]. Positive electrodes are shown in blue, and the negative electrodes are shown in red. These transmission lines, which connect the water/vacuum insulator stack to the post-hole convolute, have an effective capacitance,³³ $C_S = 8.4$ nF. The transmission lines and the post-convolute have an inductance $L_1 = 9.6$ nH. A post-hole convolute adds the currents from these levels (A-D) in parallel and delivers this current to a single feed, leading to the load. The inductance of the feed leading to the load is L_2 . Note that there is also a substantial inductance within the simulated load region, which is accounted for in the simulation.

Experiments indicate significant current losses at and down-stream of the convolute. The amount of loss increases with the initial inductance of the feed, L_F , which is the sum of L_2 and the inductance of the load region. This is because the voltage on the convolute is proportional to $L_F dI/dt$. There is evidence³⁴ that plasma forms on electrode surfaces, leading to gap closure, and thus, we expect that ion currents could be contributing to the loss. A detailed model of convolute loss has been developed.³⁵ This model successfully calculates the convolute loss for a wide variety of loads that have been tested on Z. In this model, the cathode surfaces form plasma and emit electrons when the electric field

exceeds 240 kV/cm. The current carried by electrons (flow current) is determined by the formula $I_{\text{flow}} = \frac{3}{4} \frac{V^2}{I_{\text{anode}} Z_{\text{MITL}}^2}$, where the MITL impedance is given by $Z_{\text{MITL}} = 60 \left(\frac{d_{\text{MITL}}}{r_{\text{MITL}}} \right) \Omega$, d_{MITL} is the gap, and r_{MITL} is the radius [see Fig. 2(b)]. The plasma leads to a gap closure velocity of 1.1 cm/ μs , which increases the current carried by free electrons. These electrons flow into the convolute region where some small fraction is trapped ($\sim 3\%$) by the potential well generated by ions flowing from anode to cathode surfaces. These ions are from the material desorbed from the anode surface, which consist largely of protons from water. The trapped electrons can enhance ion current above the monopolar Child-Langmuir value given by the expression $I_{\text{ion current}} = \frac{4\epsilon_0}{9} A \sqrt{\frac{2q}{m}} \frac{V^{3/2}}{d_{\text{CONV}}^2}$, where $A \sim 0.06 \text{ m}^2$ is the ion emitting surface area of the 12 posts, d is the gap between the posts and the cathode, and q and m are the charge and mass of the ions. The rest of the electron flow current is assumed to be lost to the anode before reaching the load. A large gap closure velocity (8 cm/ μs) is required within the convolute for the model to get good agreement with experiments. Although this closure velocity can be a fitting parameter, such high closure velocities have been observed experimentally.³⁴

We have developed a function based on this model, which is called at each time step of a LASNEX simulation to calculate an appropriate time-dependent value of the shunt resistor, R_s . Figure 3(a) plots the current delivered as a function of time to a standard MagLIF load with a 1 cm long liner, an outer radius of 2.79 mm, and a feed plus initial load inductance of 7.2 nH. The blue curve is the experimentally measured current, while the green curve is the simulated current without a convolute loss model. The red curve is Hutsel's detailed model,³⁵ and the black curve is from the new LASNEX model. Although not perfect, the convolute loss model is a significant improvement. The dynamic hohlraum³⁶ load has very low feed inductance (~ 3 nH) and consequently obtains high peak current on Z. The load current profiles are plotted in Fig. 3(b): the experimental curve is blue, the Hutsel model is red, and the new LASNEX model is black. This illustrates that the new LASNEX convolute loss model responds quite accurately to changes in the load inductance. Changes are larger than we propose for MagLIF experiments.

III. SIMULATIONS OF MagLIF EXPERIMENTS THAT HAVE BEEN PERFORMED ON Z

A. Clean 2D simulations

Most MagLIF experiments^{15,16} have used a feed geometry similar to that shown in Fig. 1(a) with an inductance in the range of 6.5–7.2 nH, depending on the target height. Consequently, these experiments have been driven by current pulses that peak at 16–18 MA [see Fig. 3(a)]. Similarly, the fuel density (0.7 kg/m³ of deuterium) and magnetic field strength ($B = 10$ T) have not been varied in most experiments. In contrast, the preheat energy has varied significantly. The early experiments used thick LEH windows

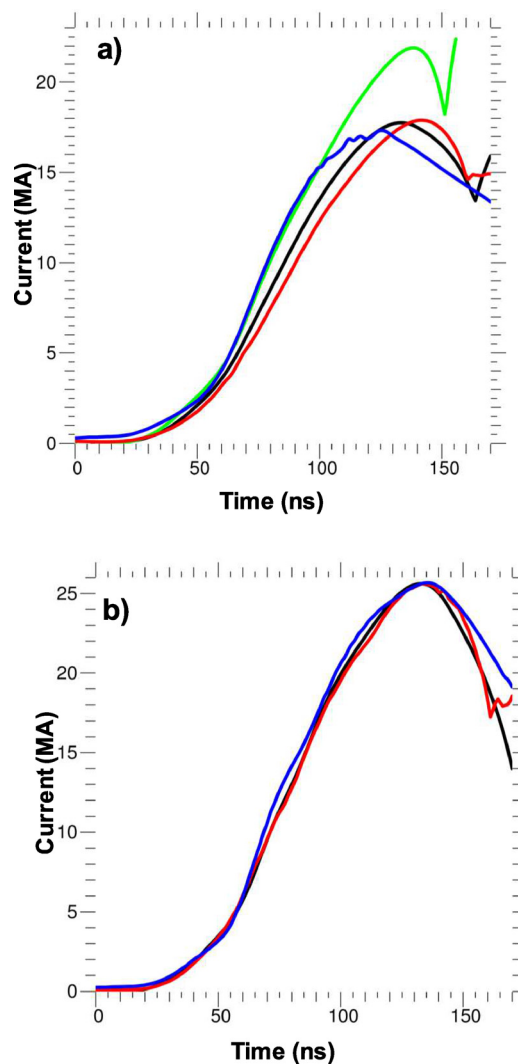


FIG. 3. Load currents are plotted as a function of time. (a) MagLIF feed with 7.2 nH and (b) dynamic hohlraum with 2.7 nH. The blue curve is from current monitors on a MagLIF experiment, the Hutsel simulation model results are red, a LASNEX simulation without convolute losses is green, and the LASNEX simulation with a new convolute model is black.

(polyimide foils $\sim 3 \mu\text{m}$ thick) and an unconditioned laser beam, so the preheat energy was only about 300 J. Later experiments used much thinner LEH windows (1.5 μm , which is just sufficient to hold the gas reliably) and phase plate smoothed laser beams (focal spot of 1.1 mm diameter), which resulted in preheat energies closer to 1 kJ. Simulated yields (a), burn averaged ion temperatures (b), pressure at peak burn (c), burn times (d), and convergence ratios (e) are plotted as a function of preheat energy in Fig. 4, with solid black curves for 10 mm liners and dotted black curves for 7.5 mm liners. The data from Z are plotted as colored symbols. Experimental data are plotted as blue squares for 10 mm tall targets with Be cushions, red squares for 10 mm targets with Al cushions, black triangles for 7.5 mm targets with Be cushions, and green triangles for 7.5 mm targets with Al cushions. Details on the analysis assumptions are provided in Appendix A.

The largest simulated yield is 8×10^{12} , which is twice the largest experimental yield for those experiments that

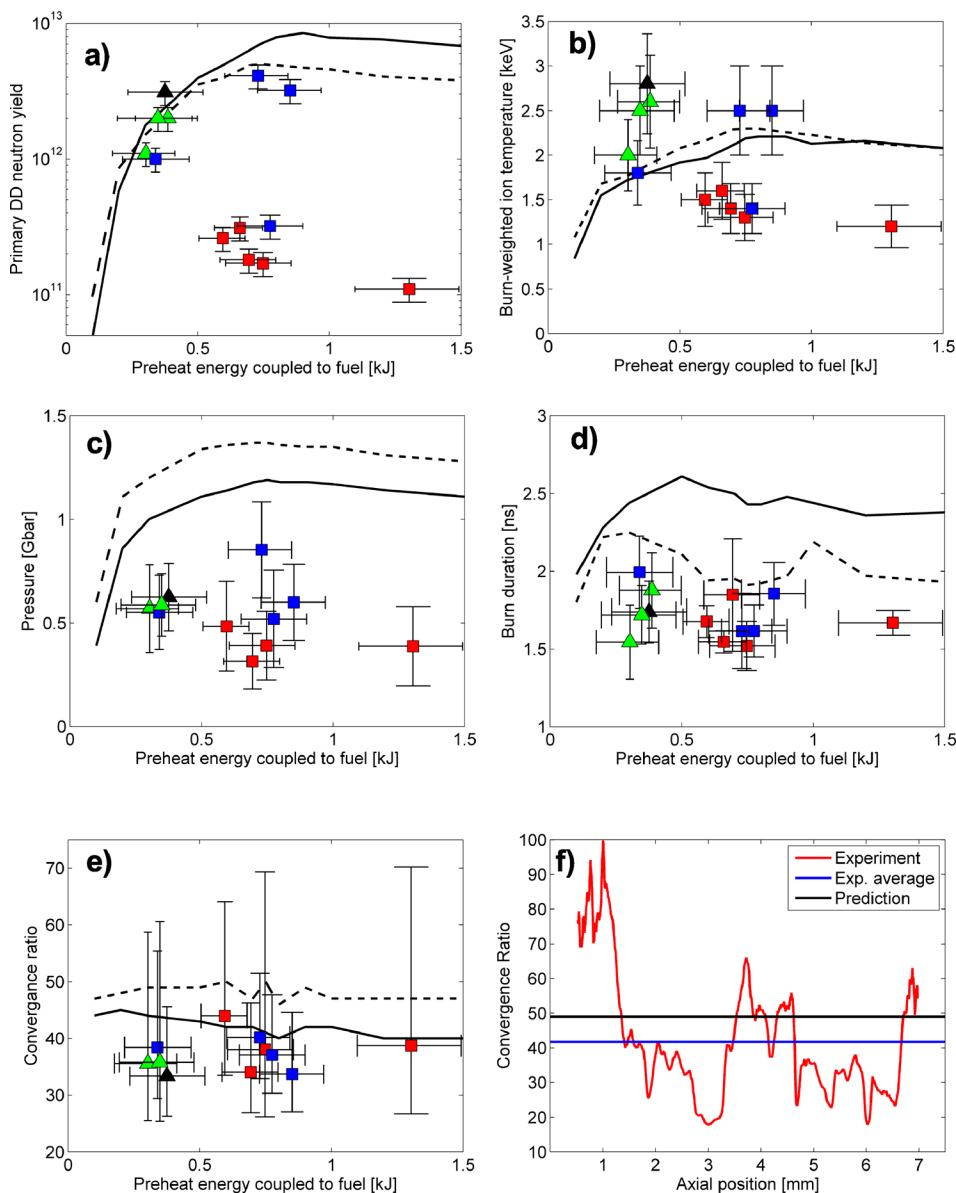


FIG. 4. Performance parameters are plotted as a function of deposited preheat energy for a peak current drive of 17.5 MA, an applied field of 10 T, and a deuterium fuel density of 0.7 kg/m^3 . (a) Neutron yield, (b) burn temperature, (c) peak pressure, (d) burn time, and (e) convergence ratio. The solid and dashed black curves represent LASNEX results for 10 mm and 7.5 mm tall targets, respectively. Experimental data are plotted as blue squares for 10 mm targets with Be cushions, red squares for 10 mm targets with Al cushions, black triangles for 7.5 mm targets with Be cushions, and green triangles for 7.5 mm targets with Al cushions. The stagnation radius for a single shot is plotted as a function of the axial position (f).

have been performed with the same parameters as our simulations. Note that higher yields have recently been obtained with higher aspect ratio liners using improved laser preheat protocols. A variation is observed in the experimental yields, some of which can be explained by intentional changes to the target design, such as a change in the target height or a change in the cushion material. However, the observed variability in yield is not always well understood. One explanation for the difference between the highest experimental result and the simulation results is mix. Mass from LEH foil could be driven into the fuel by laser heating. Such mix would enhance radiation losses from the beginning of the implosion and thus seriously affect the yield. Additionally, stochastic effects could be introduced by uncontrolled dust particles $>100 \mu\text{m}$ which could fall onto the LEH. Simulations³⁷ indicate that such particles would be driven into the fuel by laser ablation. Efforts are underway to keep the foil clean or remove it before the preheat laser fires using the laser-gate concept described in Sec. III B. The simulated and experimental burn-averaged ion temperatures (4b) are in

reasonable agreement. The experimental pressures (4c) and burn durations (4d) are less than the simulated values, which is probably due to instabilities, leading to mix and 3D effects that are not modeled. The averages of the experimentally determined convergence ratios, which are large (4e), agree reasonably well with the simulated values. The error bars for the experimental data indicate a large variation, which is not just shot to shot but the variation with the axial position within each shot as is illustrated by (4f). Although the fuel stagnation radius varies considerably ($\pm 40 \mu\text{m}$) with the axial position, it is unlikely that the liner is broken up since it is much thicker ($\sim 1000 \mu\text{m}$). However, it is quite likely that the conversion of liner kinetic energy to stagnated thermal energy is incomplete, i.e., there is residual kinetic energy in both the fuel and liner at stagnation. It is also possible that the hot fuel is not continuous over the full length of the liner due to regions of highly converged liner material. This would enhance losses from the fuel. Instability undoubtedly plays an important role in this stagnation morphology. We believe that this situation could be improved by

designing MagLIF targets to have lower convergence. We show how this can be accomplished in Sec. IV.

B. The effect of mix

Any material with an atomic number greater than 1 will enhance radiation losses in the fuel and thus lower performance. There are several ways that material could be mixed into the fuel. First, the LEH window, which absorbs a significant fraction of the laser energy, will expand rapidly and could be injected into the fuel. This is supported by observed cobalt spectral lines in experiments performed³⁸ with thin (1 nm) cobalt layers on the inside of the window. The preheated fuel also forms a blast wave which could mix the material from either the liner or the cushion. Experiments with coatings on the cushion near the LEH confirm that the cushion material is mixed into the fuel, and experiments with aluminum cushions have had lower yields than experiments with beryllium cushions. Finally, the interface between the metal liner and the fuel is unstable to the RT instability when the pressure of the fuel decelerates the liner and spectral features of iron (a liner impurity of known concentration) have been observed,³⁹ which indicate that beryllium is mixed into the fuel. This mechanism exists with all ICF approaches.

A series of 1D LASNEX simulations were performed with an initial atomic fraction of various dopants (impurities) in the fuel to study the sensitivity of MagLIF to mix. The simulated yields normalized to the clean yield (pure deuterium fuel) are plotted in Fig. 5(a). The solid curves used the best radiative cooling model,⁴⁰ i.e., Direct Configuration

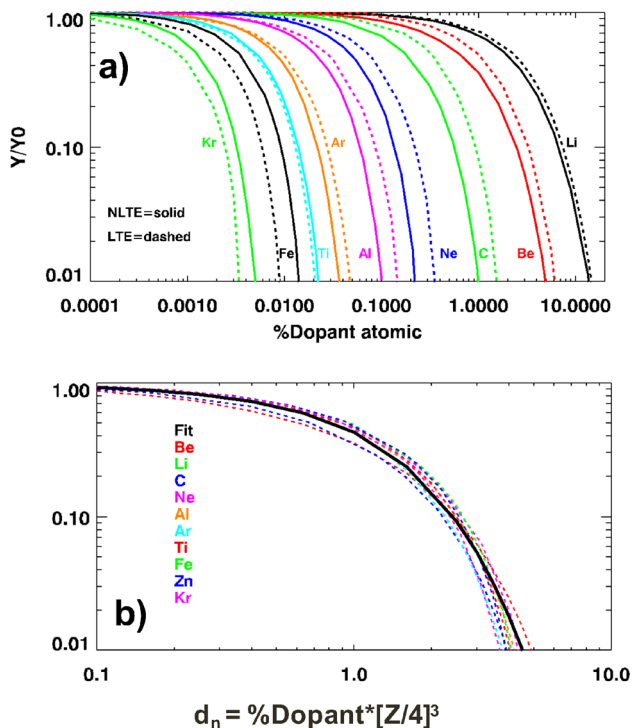


FIG. 5. (a) The ratio of the LASNEX calculated yield with a dopant over the yield without a dopant (YOC, Yield Over Clean) is plotted as a function of atomic dopant percentage. (b) The same data with the dopant scaled to account for the difference in the atomic number Z .

Accounting (DCA) with non-Local Thermodynamic Equilibrium (non-LTE). The dashed curves used an LTE model. We show both to get a sense of the dependency of these simulations on the assumed model. In addition, we compared the radiative power calculated for a fixed temperature plasma with dopants as calculated by the non-LTE DCA LASNEX model against the detailed radiation code Scram,⁴¹ with good agreement. Figure 5(a) can be used to determine the appropriate concentration of spectroscopic dopants that can be used to diagnose the fuel conditions at stagnation. As an example, krypton could be mixed into the fuel with a 0.001% atomic fraction (10 ppm) with an expected yield one half of the clean yield.

Inspection of Fig. 5(a) indicates that a beryllium atomic fraction of 2.5% should reduce the yield by a factor of 10. In comparison, it only takes an argon atomic fraction of 0.023% to reduce the yield by the same factor. Similarly, the yield will be degraded by a factor of 2 for a beryllium mix of only 0.6% or a carbon mix of 0.2%. Figure 5(b) illustrates this atomic number dependency by plotting the same data with the scaled dopant fraction $d_n = \%dopant * [Z/4]^3$.

Mix from the LEH window and the upper cushion can be introduced during the laser preheating stage as illustrated in Fig. 6(a). The laser first heats the window material, which expands rapidly jetting some material into the fuel. The laser energy then penetrates the window and heats the fuel. The heated fuel will expand radially, forming a blast wave that will first interact with the upper cushion and then impact the liner itself. Some material will most likely mix into the fuel during the blast wave interaction. The fuel heating rate and thus the blast wave strength are maximum just under the window (tunnel region) decreasing with the distance below the window, as indicated by the graded color in Fig. 6(a). This results in a net flow of material from the tunnel region into the region to be imploded by the liner. This argues that the amount of mix could increase with laser energy, unless these effects can be mitigated.

A two-pulse profile has been used to diminish this behavior. The first pulse heats the window to allow expansion to lower the density before the main pulse arrives. Nevertheless, a significant fraction of the laser energy is still absorbed by the window material, but no mix is observed. An alternative approach is to completely eliminate the window and reduce the amount of fuel within the tunnel region before the laser preheat pulse arrives. This concept, “Laser Gate,” is illustrated in Figs. 6(b) and 6(c). Several microseconds before the arrival of the laser preheat pulse, the window material is weakened so that the fuel pressure of several atmospheres breaks the window. This weakening could be accomplished with a separate laser focused to a star pattern on the top of the window as shown in Fig. 6(b). The window then opens like a gate in response to the pressure of the gaseous fuel. The gate opening time can be estimated by calculating how long it would take for the gas pressure to push the foil material a distance equal to the radius of the LEH. The result is given by the expression $t = 1.6 \times 10^{-6} \left(\frac{\Delta_\mu R_{LEH} 300 \text{ \AA}}{\rho_{fuel} T 4} \right)^{1/2}$ s, where Δ_μ is the window thickness in μm , R_{LEH} is the window radius in mm, ρ_{fuel} is the fuel density in

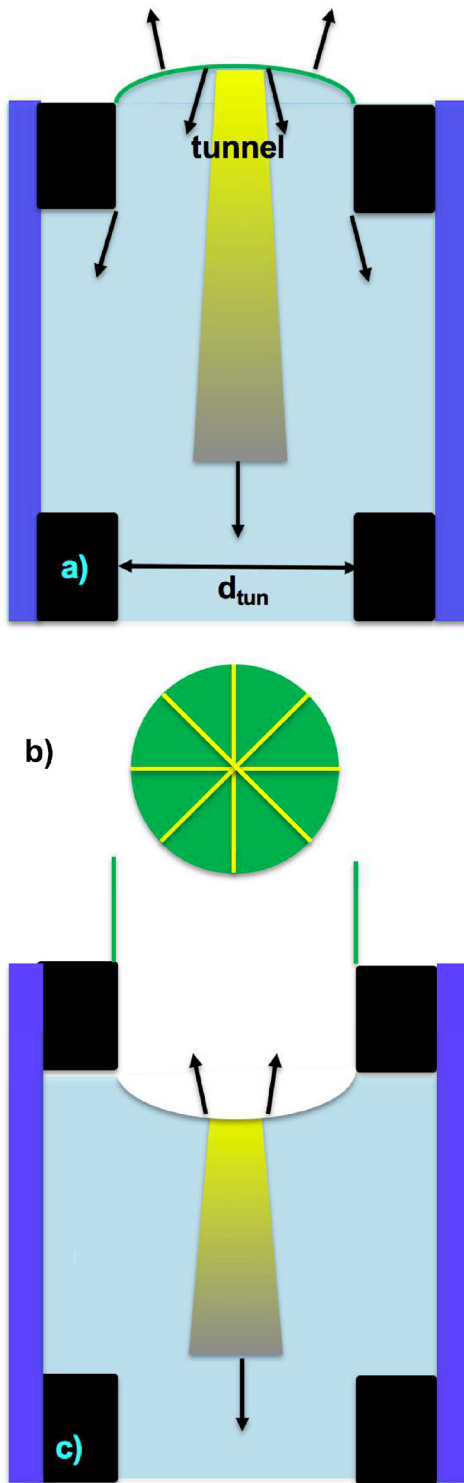


FIG. 6. A schematic of the laser-gate concept is shown: (a) The initial configuration with the LEH foil at the top, (b) top view of the LEH foil with a possible star focus pattern, and (c) the configuration after the star focus has weakened the LEH foil, the foil has burst outward (upward) and a rarefaction wave has traveled downward. The yellow trapezoid indicates the intensity of the laser deposited preheat.

kg/m^3 , T is the fuel temperature in Kelvin, and A is the mass number of the fuel molecule, i.e., $A = 4$ for deuterium and $A = 5$ for deuterium/tritium. Once the gate opens, a rarefaction wave starts propagating downward at the speed of sound, which is $c_s = 1020 \left(\frac{T}{300 \text{ \AA}} \right)^{1/2}$ m/s. The rarefaction

wave will have traveled a distance $X_r = 1.6 \left(\frac{\Delta R_{LEH}}{\rho_{fuel}} \right)^{1/2}$ mm when the gate has opened. The gas density within the tunnel estimated using the similarity solution for a planar rarefaction wave⁴² is $\rho = \rho_0 \left(1 + \frac{x-1}{4} \right)^{1/3}$, where $x = \frac{z_w - z}{X_r}$ and z_w is the axial position of the window foil. Figure 6(c) illustrates the configuration after the gate opens, and the rarefaction wave has just reached the bottom of the tunnel. The fuel density within the tunnel is less than the undisturbed fuel, which improves the laser energy delivery to the fuel that will be compressed within the liner. This configuration also has the advantage that any mix from the upper cushion will be driven upward. The Z Beamlet laser has recently been reconfigured so that a separate laser can be co-injected, and this concept will be tested soon. It has already been shown that less than 200 mJ of laser light focused in a star pattern is sufficient to break polyimide foils $> 2 \mu\text{m}$ thick. We are presently working on simulating the laser gate opening, the rarefaction wave propagation, and the flow of deuterium.

Iron spectral lines have been observed in MagLIF experiments at stagnation. Iron is an impurity of known atomic fraction (~ 110 parts/million) in beryllium that is used to fabricate the liners. These data imply a beryllium atomic fraction of about 5% at stagnation.³⁹ Inspection of Fig. 5(a) suggests at first that a 5% mix fraction would seriously degrade the yield. There are two reasons that the results shown in Fig. 5(a) might overestimate the effect of beryllium mix. The first reason is that the dopants are assumed to be mixed into the fuel before the implosion. The second reason is that the beryllium may not be mixed uniformly into the fuel. This is supported by the analysis of iron spectral line ratios, which indicate a temperature in the range of 50%–70% of the burn temperature. Note that the iron will have less effect on the yield than the beryllium due to the low impurity fraction.

To study the effect of mix timing, a series of LASNEX simulations were run with cold beryllium mixed homogeneously into the fuel at various times. The results are plotted in Fig. 7 as a function of the mix time, with the zero reference time being when the laser heating ends. The time interval between peak implosion velocity and peak burn is indicated by the vertical dashed lines. If the mix is due to the

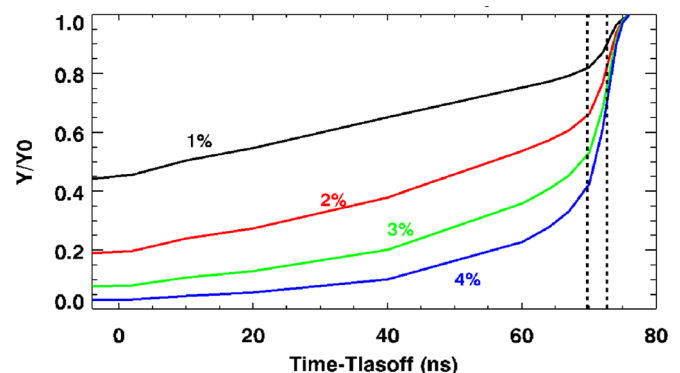


FIG. 7. The LASNEX calculated YOC with several atomic dopant concentrations is plotted as a function of the time that the dopant is introduced into the simulations.

deceleration RT instability, it would occur after peak implosion velocity, and thus, even a 4% mix would only degrade the yield by a factor of 2. Note that all of the curves rise to unity when the mix occurs after the burn is over.

To study the effect of non-uniform mix, a series of LASNEX simulations were run with cold beryllium mixed into a layer of fuel (adjacent to the inner surface of the liner) at peak velocity. The YOC (Yield Over Clean, yield with mix over the yield without mix) is plotted as a function of mix layer thickness (normalized to r_{pb} , the inner liner radius at peak burn) in Fig. 8(a) for several ratios of the total number of beryllium atoms over the total number of deuterium atoms in all of the fuel. A horizontal line at $YOC = 0.5$ is plotted for reference since the yield from 2D LASNEX simulations without mix is roughly twice the best experimental yield. A beryllium fraction of 3% mixed into all of the fuel produces $YOC = 0.5$, while progressively higher beryllium fractions are required for thinner mixing layers. Note that for thin layers (<0.25), the YOC is fairly independent of the percentage of Beryllium because the high opacity of the layer

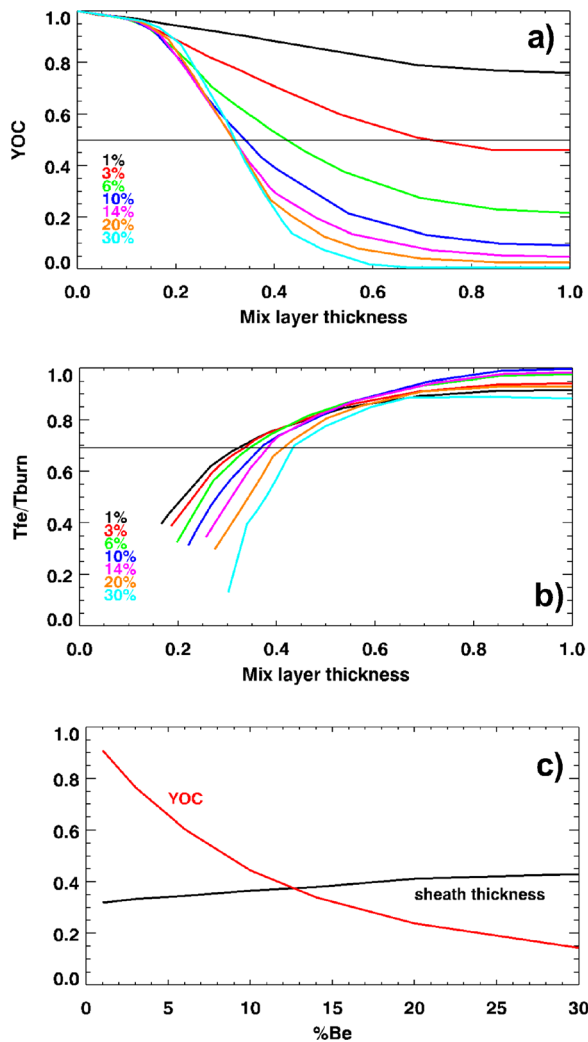


FIG. 8. LASNEX calculated (a) YOC and (b) the ratio of the iron spectroscopic inferred temperature over the burn temperature are plotted as a function of the mix layer thickness for several atomic ratios of beryllium mix to deuterium fuel. LASNEX calculated YOC and sheath thickness are plotted (c) as a function of the beryllium mix fraction for a fixed ratio $T_{fe}/T_{burn} = 0.7$.

brings it into equilibrium with the radiation temperature within the liner.

Iron was also mixed into the layer with a constant ratio of one iron atom to 9100 beryllium atoms, the impurity ratio of the experimental liners. Synthetic iron spectra were generated using the DCA non-LTE model. The line strength ratio of the helium-like resonance to the lithium-like satellite lines was used to infer electron temperature, similar to the analysis of experimental spectra from MagLIF experiments. The ratios of these inferred temperatures to the burn averaged ion temperatures (T_{fe}/T_{burn}) are plotted in Fig. 8(b). A horizontal line is plotted for reference to the experimentally measured ratio of 0.7. Note that as the normalized layer thickness approaches unity, the temperature ratio does not necessarily go to unity because the emission of iron lines and the fusion rate do not have the same temperature dependence. The YOC and mix layer thickness are plotted as a function of the beryllium percentage in Fig. 8(c), with the condition that $T_{fe}/T_{burn} = 0.7$. Then, applying the condition $YOC = 0.5$, we determine a beryllium fraction of 8.5% (in good agreement with the spectroscopic estimate of 5%) and a mix layer of 0.36.

The growth of bubbles and spikes due to the RT instability in the nonlinear regime has been shown by Dimonte⁴³ to obey the simple equation $h_i = \alpha_i A g t^2$, where h_i is the distance that either the bubble or spike has penetrated from the interface, A is the Atwood number, $(R-1)/(R+1)$, R is the ratio of the densities (heavy over light), g is the acceleration of the interface, and t is the time. For the growth of bubbles, Dimonte gives a range of values for $\alpha_B = [0.04-0.07]$ and gives the formula $\alpha_S = \alpha_B R^{0.34}$. Our LASNEX simulations indicate that $R \sim 8$, so $\alpha = (\alpha_B + \alpha_S)A = [0.1-0.18]$ and the total sheath thickness is then given by $h = \alpha g t^2$. We are interested in the growth of this sheath during the deceleration of the fuel/liner interface. This formula is equivalent to the sheath decelerating at a fraction $F_{ac} = 1 - 2\alpha$ of the interface acceleration. Using the LASNEX computed deceleration history, we find that $\alpha = 0.1$ produces a normalized mix layer thickness $h/r_{pb} = 0.36$, consistent with the mix analysis presented. This falls within the range given by Dimonte and suggests that the beryllium mixing is simply due to the deceleration RT instability.

Intuitively, we expect that reducing the convergence ratio will lead to thinner sheaths, and thus, the effect of sheath mix would be reduced. A simple current driven liner implosion model outlined in Appendix B yields a first integral of the equation of motion (EOM). The results of numerically integrating this Eq. (B1) for a convergence ratio, $C_R = 8$, are plotted in Fig. 9(a). We chose a modest convergence to make it easier to visualize. In addition to the dimensionless radius (black), velocity (blue), and current (green), the free fall line is plotted (cyan), which is the trajectory of zero acceleration extending inward from the point of maximum implosion velocity. The difference between the interface radius (black) and the free fall line (cyan) at maximum convergence is the maximum sheath thickness, h_{max} , that can be produced when $F_{ac} = 0$ ($\alpha = 0.5$). The value of h_{max} is plotted as a function of the convergence ratio in Fig. 9(b). A horizontal line is plotted at $h = 0.36$ as a reference to the results

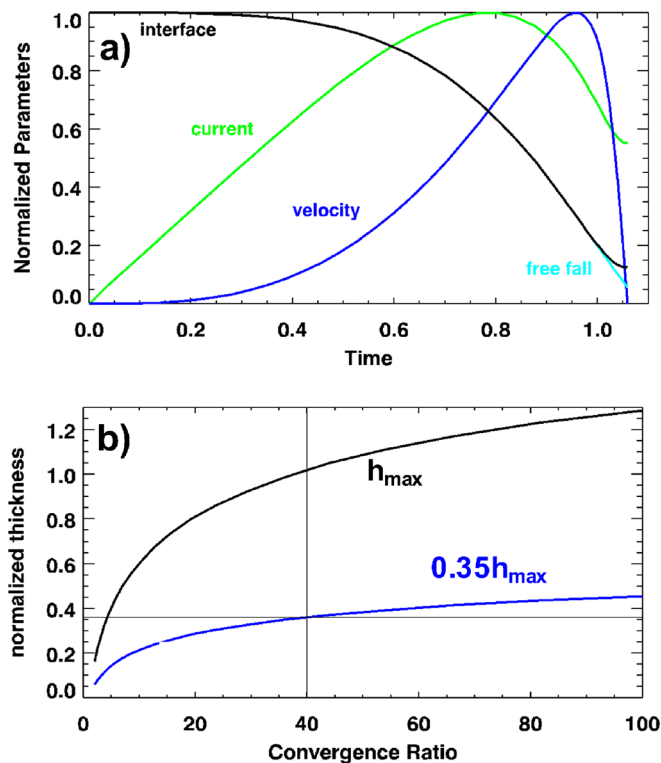


FIG. 9. (a) Dimensionless solutions from the liner implosion model [Eq. (B1)] are plotted as a function of dimensionless time. (b) The dimensionless maximum mix layer thickness is plotted as a function of the convergence ratio.

of the iron spectroscopy. LASNEX simulations indicate a convergence ratio of 40 for the present Z experiments, which is indicated by a vertical line. The blue curve obtained with $\alpha = 0.17$ ($1\text{-Fac} = 0.35$) produces a sheath, in agreement with our analysis of the iron spectral data. This is only slightly larger than the previous estimates from the Dimonte analysis, $\alpha = [0.094\text{--}0.16]$, which supports the hypothesis that the beryllium mix is due to the deceleration RT instability. Inspection of Fig. 9(b) indicates that the mixing layer thickness could be reduced by decreasing the convergence ratio.

The large variation in the stagnated fuel radius with the axial position indicates that the situation is more complex than the arguments that we have just presented. The presence of the axial magnetic field modifies the RT instability into a helical pattern, which is inherently 3D. Thus, a complete analysis will require detailed 3D simulations, which is beyond the scope of this work. The point of our analysis is to motivate that the development of a mix layer near the liner is plausible in that it can simultaneously explain the YOC and the inferred temperature from the iron spectra.

The effect of deceleration RT mix could be mitigated with an “anti-mix” layer on the inside of the liner, e.g., LiH or frozen fuel. The ability to coat the inner surface of the liner with a layer of LiH is under development. Ultimately, frozen fuel (DD or DT ice) would be the best solution because hydrogen will not increase the radiation losses. To illustrate the effectiveness of a deuterium ice antimix layer, the YOC is plotted as a function of mix layer thickness for several mix fractions in Fig. 10. The mix is beryllium for the solid curves and deuterium for the dashed curves. As can be

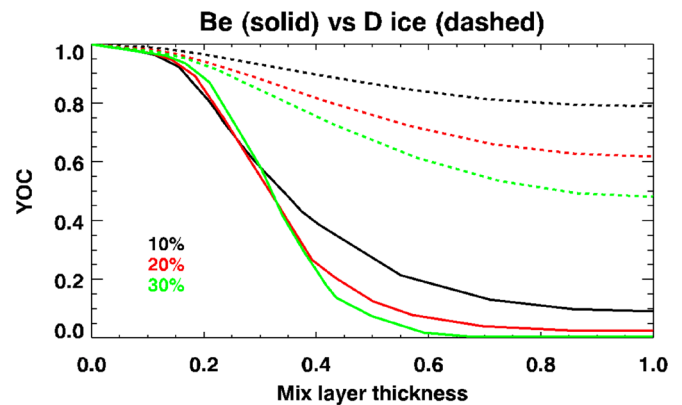


FIG. 10. LASNEX calculated YOCs are plotted as a function of mix layer thickness for several atomic mix ratios. The dopant is beryllium for the solid lines and deuterium for the dashed lines.

seen, the YOC is not strongly affected by mixing of a DT. Furthermore, developing this technique would lead naturally to high gain ice burning liners when machines with sufficient drive current become available. Capsules for laser driven ICF typically have DT ice layers, which are grown by the process^{44,45} of “beta layering.” This process could be used for MagLIF liners as well. However, at the low temperatures needed ($<18\text{ K}$) to maintain solid DT, the vapor pressure (gas density of $\sim 0.3\text{ kg/m}^3$) is substantially below the gas density needed for MagLIF liners ($>1.0\text{ kg/m}^3$). One solution is to form the ice layer and then puff gas into the liner. We have calculated that only about $15\ \mu\text{m}$ of the ice layer is melted in roughly $40\ \mu\text{s}$ it takes for this process. The details of this process will be presented in a future publication.

We now present simulations to show how MagLIF performance could be improved on the existing Z machine. We assume that the effect of mix is mitigated by using an ice antimix layer, and thus, these simulations will not include the effect of mix.

IV. SIMULATIONS OF MagLIF EXPERIMENTS THAT CAN BE PERFORMED ON Z

A. Performance with existing power feed and drive current

A series of 2D LASNEX simulations were run to show that MagLIF performance could be substantially improved, without increasing the drive current, by increasing the axial magnetic field, the preheat energy, and the fuel density. In all the simulations, we assumed deuterium fuel, a standard MagLIF feed with an inductance of $7.2\ \text{nH}$, and a beryllium liner $1\ \text{cm}$ in length with an outer radius of $2.79\ \text{mm}$ and an aspect ratio of 6 (i.e., an inner radius of $2.3\ \text{mm}$). Consequently, all of these simulations had a peak current of $17.5\ \text{MA}$. The results are plotted in Fig. 11: (a) neutron yield as a function of preheat energy deposited in the fuel, (b) convergence ratio as a function of fuel density (at the preheat energy that optimized yield), and (c) fuel gain (assuming DT fuel) as a function of a generalized Lawson parameter (described later).

Each color in Fig. 11(a) corresponds to a different fuel density, while each curve is labeled with the axial magnetic field strength. Field strengths in excess of $30\ \text{T}$ may be

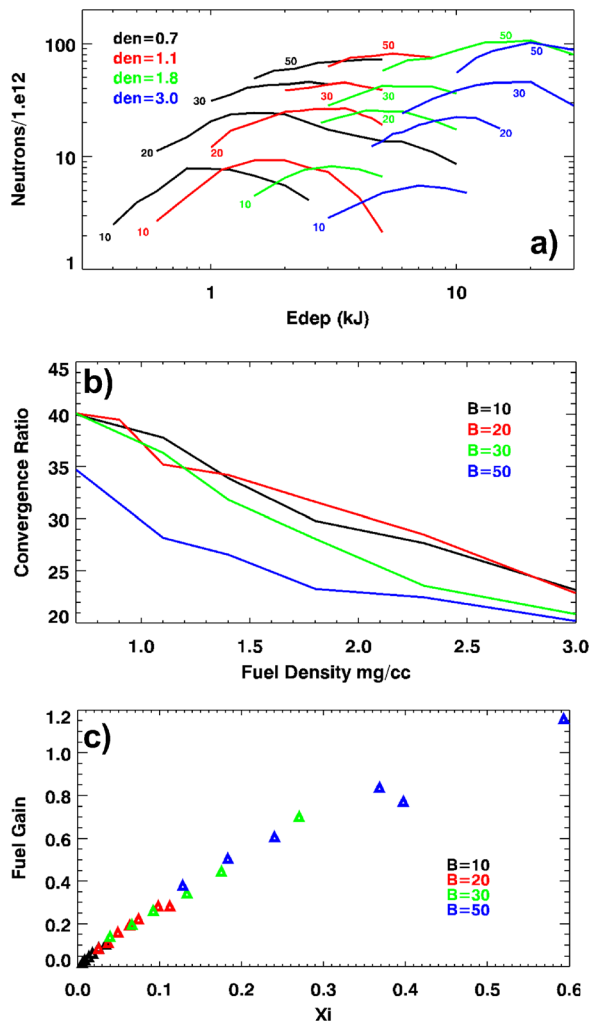


FIG. 11. (a) LASNEX calculated neutron yields are plotted as a function to the deposited preheat energy. The colors (black, red, green, and blue) are for fuel densities (0.7, 1.1, 1.8, and 3.0) kg/m^3 , respectively. Each curve is labelled with the applied axial magnetic field. (b) The LASNEX calculated convergence ratio is plotted as a function of fuel density. The colors are for different applied magnetic fields. The preheat energy that produced maximum yield was used for each point. (c) The LASNEX calculated fuel gain from simulations with deuterium/tritium fuel is plotted as a function of the Lawson parameter X_i described in the text.

impractical with external field coils, but an alternate concept^{46,47} could produce fields greater than 50 T. The MagLIF experiments have been performed used an initial fuel density of 0.7 kg/m^3 , which is the fuel density of the black curves. These curves indicate that the yield is increased significantly with the increased magnetic field and that there is an optimum preheat energy that increases with field strength. Even at the largest field strengths, electron thermal conduction is the dominant heat loss mechanism within the hot fuel. Thus, increasing the field reduces losses and increases the yield. A higher initial field also reduces the Nernst effect which advects the magnetic field out of the central hot region. Too much preheat increases the fraction of the initial magnetic field that is advected out of the hot spot, and thus, there is an optimum preheat level. Inspection of all the curves reveals that there is an optimum density for each field strength and that the optimum preheat increases with fuel density, i.e., the optimum average preheat temperature is nearly constant (100–200 eV).⁴

We define the convergence ratio as the ratio of the liner/fuel interface radii at $t = 0$ and at peak burn. Simulations and experiments indicate convergence ratios of about 40 for the MagLIF experiments that have been executed on Z. Images at stagnation have a structure indicating that the hot fuel may be filamented by a flute instability, and thus, we would like to decrease the convergence ratio. Simulations show that the convergence ratio is most strongly affected by the initial fuel density as shown in Fig. 11(b). Figures 11(a) and 11(b) indicate that the fuel density, an initial B-field, and the preheat energy need to be increased for improved performance, with modest convergence. The frequency doubled Z Beamlet laser has a critical density of 14 kg/m^3 in deuterium. LPI should be controlled by keeping the fuel density to $1/10^{\text{th}}$ of the critical density,⁴⁸ i.e., a deuterium density of 1.4 kg/m^3 . Inspection of Fig. 11(b) reveals that this density will only moderately improve the convergence. If LPI becomes a problem above this density, it may be necessary to frequency triple, which would raise the critical density to 31 kg/m^3 and fuel densities as high as 3 kg/m^3 could be used with a substantial reduction in the convergence ratio.

Procedures are being developed to allow the Z machine to use DT fuel. In the interim, a generalized Lawson parameter^{49,50} of the form, $X_i = S(T)P\tau$, can be used to determine performance, where $S(T)$ is given by the expression $S(T) = 3.17 \times 10^5 T^{-2.4} e^{(-19.94T^{-0.33})}$. This Lawson parameter was determined from each of the simulations shown in Fig. 11(a). A second series of simulations were performed with DT fuel at densities scaled by the factor of 5/4 to keep the number density the same. The DT simulations were used to calculate the fuel gain, which we define as the yield divided by the maximum fuel energy without burn. The DT gain is plotted as a function of X_i in Fig. 11(c). There is a high correlation, so X_i can be used to calculate the DT-equivalent fuel gain from the measurable quantities of MagLIF experiments with deuterium fuel. This would be corroborated by simulations with DD and DT fuel.

In Sec. IV B, we discuss how the drive current can be increased to a MagLIF load on the Z machine. Without improving the initial fuel conditions, this will result in increased convergence, i.e., >40 . We emphasize that increased drive current will only improve MagLIF performance if the initial fuel conditions are modified to keep the convergence ratio reasonable, i.e., <40 .

B. Increasing the drive current

Simulations indicate that MagLIF yields increase with increasing drive current when the fuel conditions (density, preheat energy, and B-field) are optimal. The drive current delivered by Z can be significantly increased by reducing the feed inductance and raising the Marx charge voltage, as illustrated in Fig. 12. This is a plot of the peak current as a function of feed inductance for different values of the Marx voltage as calculated using the LASNEX convolute loss model described in Sec. II and fixed initial dimensions of the MagLIF load. The optimal liner radius increases with drive current but by a very small amount ($<5\%$) over this range of currents.

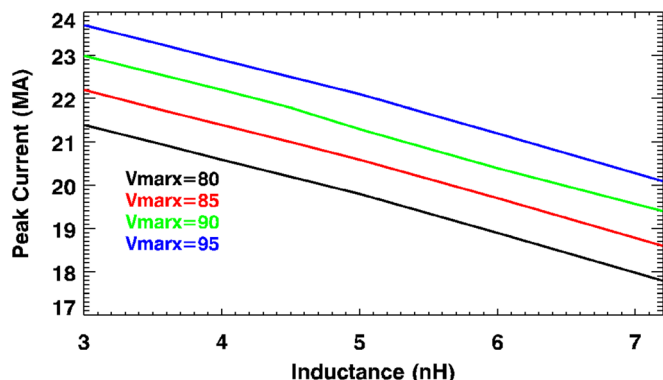


FIG. 12. LASNEX calculated currents using the convolute loss model are plotted as a function of the initial inductance for several values of the Marx charge voltage.

Most of the experiments that have been performed on Z have used a Marx voltage of 80 kV with the standard MagLIF feed (7.2 nH) and thus had a peak current of 17.5 MA. Figure 12 indicates that the current could be increased by simply increasing the Marx voltage. However, this will raise the voltage on the vacuum/water interface (stack), which could cause the stack to breakdown early enough to affect the current delivery or even cause expensive damage. Reducing the feed inductance lowers the voltage at the stack, and thus, the Marx voltage can be raised without damage.

A significantly lower feed inductance (4.5 nH) can be obtained with the modification of the field coils as shown in Fig. 13. This results in a drive current of about 21 MA by assuming a Marx charge voltage of 90 kV. Even higher currents will be possible using the AutoMag concept,^{46,47} which removes the need for field coils altogether. The field is generated by a helical composite liner using the early part of the

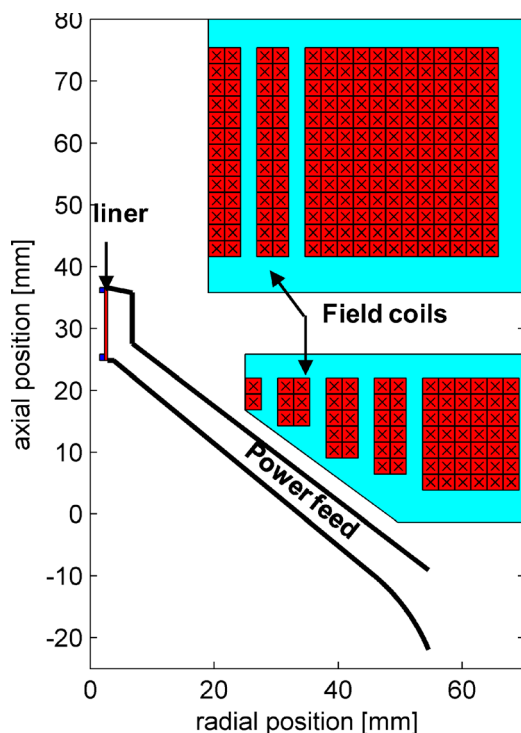


FIG. 13. A schematic of a new field coil design allowing a low feed inductance.

drive current. Without field coils, the feed inductance can be further reduced to 3.5 nH. Simulations with the convolute loss model indicate a peak drive current of 22.6 MA for a Marx charge of 95 kV.

Figure 14(a) is a plot of the simulated yields as a function of the initial axial field for the three feed inductances and peak drive currents. The fuel was assumed to be deuterium/tritium at a density of 1.87 kg/m³, which is approximately 1/10th of the critical density for the existing frequency doubled Z Beamlet laser. The preheat energy was

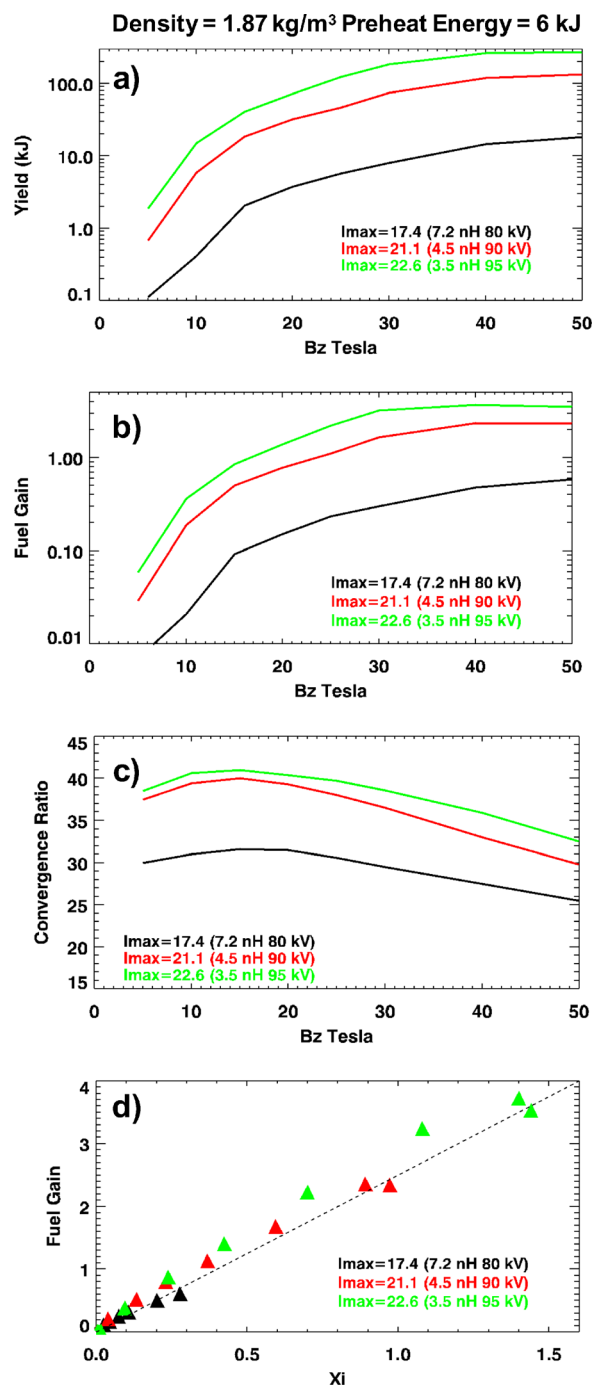


FIG. 14. LASNEX calculated (a) fusion yields, (b) fuel gain, and (c) convergence ratios are plotted as a function of the initial axial magnetic field for several values of the initial feed inductance. A preheat of 6 kJ into a deuterium/tritium fuel at a density of 1.87 kg/m³ was assumed. (d) The fuel gain plotted as a function of the Lawson parameter.

assumed to be 6 kJ, which the Z Beamlet could provide with some modest modifications. The yields vary by more than a factor of 100, which indicates that considerable MagLIF scaling information is obtainable on the existing Z machine. The fuel gain shown in Fig. 14(b) has a similar variation and can exceed unity by a significant margin. The fuel gain is plotted as a function of the generalized Lawson Parameter in Fig. 14(d). This plot would allow MagLIF experiments with deuterium fuel to be scaled to a DT equivalent fuel gain. The convergence ratios plotted in Fig. 14(c) vary from 30 to 40 for magnetic fields that can be produced by external field coils (<30 T). One might expect good agreement between simulated and experimental yields when the convergence ratio is modest. Experiments will be possible to determine if there is a maximum convergence ratio above which the simulations and experiments disagree. Dielectric coatings on the outside surface of MagLIF liners have been shown to improve the stability of the implosion^{13,14} by inhibiting the

electro-thermal instability. Such coatings may allow MagLIF liners to be imploded to higher convergence ratios without performance degradation. If it is found that, even with coatings, the convergence ratio is too high to take advantage of the highest current that can be delivered by the Z machine, the convergence ratios can be reduced by going to higher fuel densities. Figure 15 shows the same information as Fig. 14 but with a fuel density of 3.75 kg/m³, which corresponds to 1/10th critical for a frequency tripled laser. The preheat energy was assumed to be 4 kJ to account for losses in converting frequency doubled to frequency tripled light. The convergence ratios are reduced but so are the yields and gains due to the lower preheat energy. It must be remembered that Z Beamlet was built to provide x-ray backlighting and not as a preheat source for MagLIF. However, it has been used successfully to demonstrate the principles of MagLIF and is sufficient to provide considerable scaling.

We performed an additional set of simulations by assuming a fuel density of 3.75 but increasing the preheat energy above what could be provided by Z Beamlet. The fusion yields are plotted as a function of the preheat energy in Fig. 16(a),

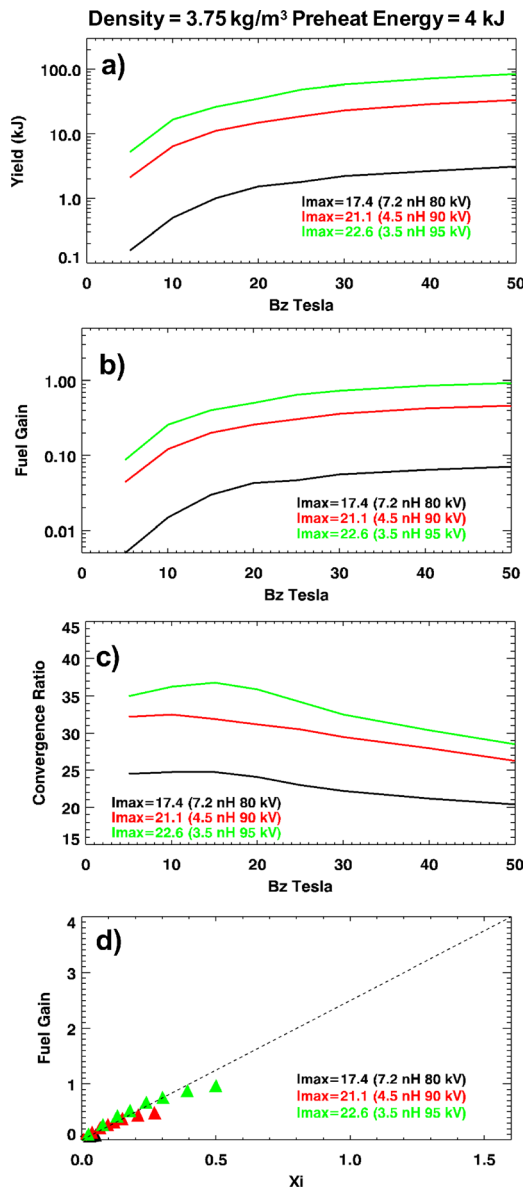


FIG. 15. The same as Fig. 14, but the fuel density was 3.75 kg/m³ and the preheat energy was 4 kJ.

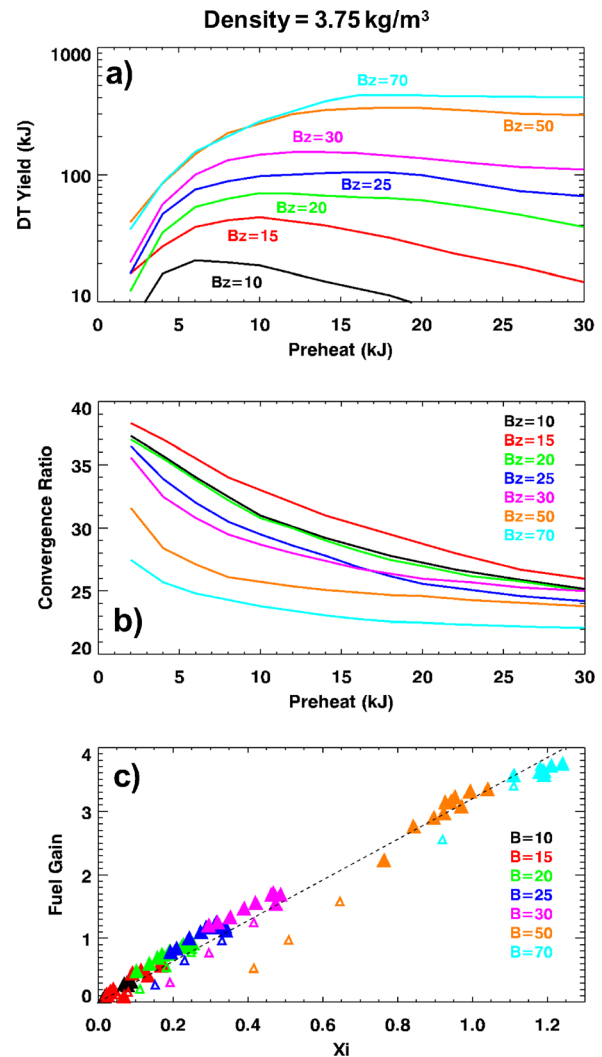


FIG. 16. LASNEX calculated (a) fusion yields and (b) convergence ratios are plotted as a function of the fuel preheat for several values of the initial axial magnetic field. The fuel density was 3.75 kg/m³. (c) The fuel gain plotted as a function of the Lawson parameter.

the convergence ratios are plotted as a function of the fuel preheat energy in Fig. 16(b), and the fuel gains are plotted as a function of the Lawson parameter in Fig. 16(c). The small symbols are for simulations with less than 60% of the optimum preheat. The results indicate a substantial improvement in MagLIF performance at higher preheat energies if axial B fields greater than 30 T can be provided. This might be possible with the AutoMag concept.

V. DISCUSSION AND CONCLUSIONS

We have compared the results of 2D LASNEX simulations of MagLIF to the experiments that have been performed on the Z machine. These calculations, which included a model of the current loss at the convolute, have simulated drive currents, in good agreement with the measured currents. The simulated neutron yields are roughly twice the best experimental results, i.e., $YOC \sim 0.5$. Spectroscopic measurements indicate that the material from both the LEH foil and the beryllium liner is mixed into the fuel before stagnation. Note that the LEH material could be mixed into nearly all of the fuel early in the implosion, while the liner material is probably mixed into a sheath during deceleration. We presented simulations of the yield degradation from various materials mixed into the fuel and showed that the effect is proportional to the cube of the atomic number. The mix from the LEH foil depends on the laser heating pulse shape and intensity, and it could be completely eliminated by using the Laser-gate concept. The beryllium mix is most likely due to the Rayleigh-Taylor instability during the deceleration of the liner by the fuel pressure. The liner mix is estimated from the iron impurity within the beryllium. The temperature inferred from the iron spectra is 50%–70% of the burn temperature inferred from neutron time of flight. We have used a ratio of 70% and $YOC = 0.5$ to determine that the fuel layer mixed with beryllium has a thickness of ~ 0.36 of the liner interface radius at peak burn and the total number of beryllium atoms mixed into the fuel is about 8.5% of the initial fuel atoms. Note that we used the higher ratio of the temperatures since this would imply a larger mix layer. A simple model of a magnetically driven liner has been presented, which showed that the maximum thickness of the mix layer due to the deceleration RT instability increases monotonically with the convergence ratio and that our inferred mix layer thickness is consistent with published models of the nonlinear growth of the RT instability. We presented simulations showing that coating the inner surface of the liner with deuterium or DT ice would mitigate the performance degradation due to mix.

We then presented simulations, indicating that yields much larger than have been produced so far on Z could be obtained without increasing the drive current, just by increasing the fuel density, preheat energy, and magnetic field. Lower convergence ratio implosions are more robust to drive asymmetries and the RT instability. These simulations indicate that the convergence ratio is most affected by the fuel density. We then showed that the DT equivalent fuel gain can be determined from deuterium experiments using a generalized Lawson criterion.

Further improvements to the yield could be obtained by increasing the drive current. We presented simulations using the convolute loss model which indicate that higher drive currents are possible by lowering the initial feed inductance and raising the Marx charge voltages. A field coil and feed design are presented, which would increase the applied magnetic field and reduce the feed inductance. We then presented simulations of MagLIF performance as a function of the applied magnetic field with several values of the feed inductance, Marx voltage, and two values of the fuel density.

A preheat energy of 6 kJ was assumed for the lower fuel density cases (1.87 kg/m^3). This is about the energy that the existing Z Beamlet laser could produce with green light. High yields ($\sim 100 \text{ kJ}$ for DT) and fuel gains are indicated, but the convergence ratios are high (~ 40). Higher fuel density implosions would have lower convergence ratios, but Laser Plasma Instabilities could be a problem unless Z Beamlet was converted to blue light. This would lower the available laser energy to about 4 kJ. Simulations indicate not only lower convergence ratios but also a substantial reduction in yield and gain due to the lower preheat energy, which suggests that a laser upgrade would be desirable. Simulations indicate that substantial yield improvements should continue up to preheat energies of 10–20 kJ.

The results presented indicate that significant scaling of the MagLIF concept could be explored on the existing Z machine and plans are underway to test these predictions. Experimental confirmation of this predicted scaling on Z would reduce the risk of scaling to a future machine.

ACKNOWLEDGMENTS

Sandia National Laboratories is a multimission laboratory managed and operated by the National Technology and Engineering Solutions of Sandia, LLC, a wholly owned subsidiary of Honeywell International, Inc., for the U.S. Department of Energy's National Nuclear Security Administration under Contract No. DE-NA-0003525. This paper describes objective technical results and analysis. Any subjective views or opinions that might be expressed in the paper do not necessarily represent the views of the U.S. Department of Energy or the U.S. Government.

APPENDIX A: UNDERSTANDING MagLIF EXPERIMENTAL CONDITIONS

The four key inputs in MagLIF are the applied B-field, laser energy deposition, initial fuel density, and load current. The load current measured by B-dot monitors is in good agreement with a circuit model,³⁵ which was adapted into LASNEX. The applied axial B-field is measured using a B-dot loop just above the applied B-field coils.⁵¹ The laser energy deposited in the fuel is not measured directly, but the energy exiting the laser is measured on each experiment. A method to approximate the energy deposition in the fuel is based on this measurement, and an energy balance was developed. The method accounts for (1) energy lost due to imperfect optics between the laser and the target, (2) energy absorbed in the laser entrance hole foil, which is used to

retain the fuel, (3) energy backscattered due to stimulated Brillouin backscattering, and (4) energy scattered outside of the incident beam cone but retained within the fuel. Experiments conducted in a separate target chamber²⁹ were used to estimate points 2–4. This analysis assumes that the energy lost to stimulated Raman scattering is small compared to the other losses and that the energy lost to the foil does not significantly change when a 10T field is applied. The uncertainty in the estimate represents ± 1 sigma based on the uncertainty in (1) the optical chain transmission, (2) the beam spot size, (3) the laser entrance hole window thickness, (4) the transmission dataset, and (5) the stimulated Brillouin backscatter dataset.

Several key parameters were used to evaluate the experimental stagnation performance. The main measurements were primary neutron yield, ion temperature, burn duration, and plasma radius. These stagnation conditions were inferred using a series of x-ray and neutron diagnostics, which are typically fielded on all MagLIF experiments.

The primary deuterium-deuterium neutron yield has been described. The burn-weighted ion temperature is determined using a forward-fit in time-space to the neutron time of flight (NTOF) spectrum. Approximately, the first two-thirds of the peak is used to infer the temperature; the late-time data are ignored due to significant neutron scatter broadening. While up to five NTOF spectra are recorded on each shot, the front detector at the line of sight 270 has the best collimation/cleanest signal. The Ballabio model²³ is used to determine the ion temperature from this spectrum. Similar to the activation measurement, the uncertainty in the ion temperature measurement is 20% and is dominated by neutron scattering.

The Z facility does not have a true burn duration diagnostic, but simulations indicate that the x-ray emission duration is a good surrogate for the burn duration, and thus, the full-width at half-maximum of the experimental x-ray diode traces was used to estimate the burn duration. The x-ray duration was measured using Photo Conducting Detectors (PCD) and SiDs⁵² with various x-ray filters. No significant difference in the width was observed between soft-filtered channels (2–5 keV) and hard-filtered channels (10–15 keV). The uncertainty in the burn duration approximation is given by the standard deviation in the widths determined from up to six diodes in each experiment.

The convergence ratio was approximated using a time-integrated spherical crystal image.⁵³ A convolution of the instrument point-spread-function and an assumed plasma profile were forward-fit to the experimental data to estimate the plasma radius. Based on simulations, the plasma pressure was assumed to be constant with a radial temperature profile of $T(r) = T_{peak}[1 - (1 - \frac{T_{rad}}{T_{peak}})\xi^4]$, where T_{peak} is the temperature on axis, T_{rad} is the temperature at the edge of the plasma (assumed to be $0.1T_{peak}$), and ξ is the radial position in the plasma normalized to the plasma radius. A fixed T_{peak} consistent with the measured burn-weighted T_{ion} was assumed, and at each axial location, the plasma radius was determined. The mean plasma radius and the plasma volume were calculated based on the radius as a function of the axial position. To check for sensitivity to the model, the

calculation was repeated for temperature at $T_{ion} \pm 1$ sigma and with the radial position exponent set to 3 and 5. The change in the mean plasma radius with these variations was much smaller than the variation in the plasma radius over the height of the stagnation column. The convergence ratio is given as the initial fuel-liner boundary (2.325 mm) over the mean plasma radius with the uncertainty dominated by the axial variation in the plasma radius. Note that the crystal imager was not successfully fielded on all experiments, so the convergence ratio and plasma volume could not be determined for all experiments.

The plasma pressure was estimated by assuming the same isobaric model as in the convergence ratio calculation. The mix fraction was assumed to be uniformly $3 \pm 2\%$ with an effective atomic number of 5. Given the burn-weighted ion temperature, burn duration, and plasma volume, the plasma pressure was determined by matching the primary neutron yield. The uncertainty in the pressure inference is a combination of the uncertainty in the ion temperature, burn duration, plasma volume, and primary neutron yield. The plasma pressure could not be estimated for the experiments in which the plasma volume was not determined.

APPENDIX B: A SIMPLE LINER IMPLOSION MODEL

Assuming that the liner is of infinitesimal thickness, the implosion trajectory is given by the equation $M \frac{d^2 r}{dt^2} = 2\pi r L P$, where r is the liner radius, M and L are the liner mass and length, P is the sum of the internal gas pressure, P_G , and the exterior magnetic pressure, P_M . Due to the preheat and slow implosion velocity of MagLIF liners, the gas pressure is given approximately by the simple formula $P_G = P_0 (\frac{\rho}{\rho_0})^\gamma$. After preheat, the deuterium or DT fuel will no longer be diatomic, so γ would be $5/3$ for an adiabatic implosion. In practice, there is significant loss of energy during the implosion due to both thermal conduction and radiation, which can be approximately accounted for by using a reduced value of γ . Choosing the mathematically convenient value, $\gamma = 1.5$, ignoring gas losses out the ends of the liner, and forcing the gas pressure to be zero until the liner starts to implode, we obtain $P_G = P_0 [x^{-2} - 1]$, where $x = r/r_0$, r_0 is the initial radius of the liner. The magnetic pressure is given by the expression, $P_M = -\frac{\mu_0 I^2}{8\pi^2 r^2}$, where the drive current, I , is a function of time. We choose the specific form $I^2 = 1.5\sqrt{3}x(1-x)^{1/2}I_0^2$, which has the important features of realistic current profiles, namely, it starts at zero ($x=1$), rises to the maximum I_0 ($x=2/3$), and then falls. Combining these equations, we obtain the equation of motion (EOM), $\frac{d^2 x}{dt^2} = A_M [Q(x^{-2} - 1) - (1-x)^{1/2}]$, where $A_M = -\frac{3\sqrt{2}L\mu_0 I_0^2}{8\pi r_0^2 M}$ and $Q = \frac{2\pi P_0}{A_M}$. We set $Q=0$ and integrate the EOM twice to obtain a reference implosion time $t_0 = (\frac{12}{A_M})^{1/2}$, which we use to define a dimensionless time variable, $\tau = \frac{t}{t_0}$. The EOM is then put into the dimensionless form $\frac{d^2 x}{d\tau^2} = \ddot{x} = 12[Q(x^{-2} - 1) - (1-x)^{1/2}]$. The first integral is

$$\dot{x} = -\left\{24 \left[Q \left(2 - x - \frac{1}{x}\right) + \frac{2}{3}(1-x)^{3/2}\right]\right\}^{1/2}. \quad (B1)$$

The velocity goes to zero at the minimum value of x defined to be x_n , which is the reciprocal of the convergence ratio

$$C_{R,Q} \text{ is related to } x_n \text{ by the expression } Q = -\frac{2(1-x_n)^{3/2}}{3(2-x_n-1/x_n)}.$$

- ¹J. Lindl, *Phys. Plasmas* **2**, 3933 (1995).
- ²I. R. Lindemuth and R. C. Kirkpatrick, *Nucl. Fusion* **23**, 263 (1983).
- ³I. R. Lindemuth and M. M. Widner, *Phys. Fluids* **24**, 746 (1981).
- ⁴S. A. Slutz, M. C. Herrmann, R. A. Vesey, A. B. Sefkow, D. B. Sinars, D. C. Rovang, K. J. Peterson, and M. E. Cuneo, *Phys. Plasmas* **17**, 056303 (2010).
- ⁵S. A. Slutz and R. A. Vesey, *Phys. Rev. Lett.* **108**, 025003 (2012).
- ⁶M. E. Cuneo, M. C. Herrmann, D. B. Sinars, S. A. Slutz, W. A. Stygar, R. A. Vesey, A. B. Sefkow, G. A. Rochau, G. A. Chandler, J. E. Bailey *et al.*, *IEEE Trans. Plasma Sci.* **40**, 3222 (2012).
- ⁷P. K. Rambo, I. C. Smith, J. L. Porter, Jr., M. J. Hurst, C. S. Speas, R. G. Adams, A. J. Garcia, E. Dawson, B. D. Thurston, C. Wakefield *et al.*, *Appl. Opt.* **44**, 2421 (2005).
- ⁸D. B. Sinars, S. A. Slutz, M. C. Herrmann, R. D. McBride, M. E. Cuneo, C. J. Jennings, J. P. Chittenden, A. L. Velikovich, K. J. Peterson, R. A. Vesey *et al.*, *Phys. Rev. Lett.* **105**, 185001 (2010).
- ⁹D. B. Sinars, S. A. Slutz, M. C. Herrmann, R. D. McBride, M. E. Cuneo, K. J. Peterson, R. A. Vesey, C. Nakhleh, B. E. Blue, K. Killebrew *et al.*, *Phys. Plasmas* **18**, 056301 (2011).
- ¹⁰R. D. McBride, S. A. Slutz, C. A. Jennings, D. B. Sinars, M. E. Cuneo, M. C. Herrmann, R. W. Lemke, M. R. Martin, R. A. Vesey, K. J. Peterson *et al.*, *Phys. Rev. Lett.* **109**, 135004 (2012).
- ¹¹R. D. McBride, M. R. Martin, R. W. Lemke, C. A. Jennings, D. C. Rovang, D. B. Sinars, M. E. Cuneo, M. C. Herrmann, S. A. Slutz, C. W. Nakhleh *et al.*, *Phys. Plasmas* **20**, 056309 (2013).
- ¹²T. J. Awe, C. A. Jennings, R. D. McBride, M. E. Cuneo, D. C. Lamppa, M. R. Martin, D. C. Rovang, D. B. Sinars, S. A. Slutz, A. C. Owen *et al.*, *Phys. Plasmas* **21**, 056303 (2014).
- ¹³K. J. Peterson, T. J. Awe, E. P. Yu, D. B. Sinars, E. S. Field, M. E. Cuneo, M. C. Herrmann, M. Savage, D. Schroen, K. Tomlinson, and C. Nakhleh, *Phys. Rev. Lett.* **112**, 135002 (2014).
- ¹⁴T. J. Awe, K. J. Peterson, E. P. Yu, R. D. McBride, D. B. Sinars, M. R. Gomez, C. A. Jennings, M. R. Martin, S. E. Rosenthal, D. G. Schroen, A. B. Sefkow, S. A. Slutz, K. Tomlinson, and R. A. Vesey, *Phys. Rev. Lett.* **116**, 065001 (2016).
- ¹⁵M. R. Gomez, S. A. Slutz, A. B. Sefkow, D. B. Sinars, K. D. Hahn, S. B. Hansen, E. C. Harding, P. F. Knapp, P. F. Schmit, C. A. Jennings *et al.*, *Phys. Rev. Lett.* **113**, 155003 (2014).
- ¹⁶M. R. Gomez, S. A. Slutz, A. B. Sefkow, K. D. Hahn, S. B. Hansen, P. F. Knapp, P. F. Schmit, C. L. Ruiz, D. B. Sinars, E. C. Harding *et al.*, *Phys. Plasmas* **22**, 056306 (2015).
- ¹⁷K. D. Hahn, G. W. Cooper, C. L. Ruiz, D. L. Fehl, G. A. Chandler, P. F. Knapp, R. J. Leeper, A. J. Nelson, R. M. Smelser, and J. A. Torres, *Rev. Sci. Instrum.* **85**, 043507 (2014).
- ¹⁸C. L. Ruiz, G. W. Cooper, S. A. Slutz, J. E. Bailey, G. A. Chandler, T. J. Nash, T. A. Mehlhorn, R. J. Leeper, D. Fehl, A. J. Nelson, J. Franklin, and L. Ziegler, *Phys. Rev. Lett.* **93**, 015001 (2004).
- ¹⁹R. J. Leeper, C. L. Ruiz, G. A. Chandler, G. W. Cooper, D. E. Bower, D. N. Fittinghoff, E. C. Hagen, J. R. Hollaway, I. J. McKenna, L. A. McPherson *et al.*, *J. Phys.: Conf. Ser.* **112**, 032076 (2008).
- ²⁰K. D. Hahn, G. A. Chandler, C. L. Ruiz, G. W. Cooper, M. R. Gomez, S. A. Slutz, A. B. Sefkow, D. B. Sinars, S. B. Hansen, P. F. Knapp *et al.*, *J. Phys.: Conf. Ser.* **717**, 012020 (2016).
- ²¹T. Goorley, "MCNP6.1.1-Beta Release Notes," LA-UR-14-24680 (2014).
- ²²A. J. Harvey-Thompson, private communication (2018).
- ²³L. Ballabio and G. Gorini, *Nucl. Fusion* **38**, 1723 (1998).
- ²⁴S. B. Hansen, M. R. Gomez, A. B. Sefkow, S. A. Slutz, D. B. Sinars, K. D. Hahn, E. C. Harding, P. F. Knapp, P. F. Schmit, T. J. Awe *et al.*, *Phys. Plasmas* **22**, 056313 (2015).
- ²⁵P. F. Schmit, P. F. Knapp, S. B. Hansen, R. R. Gomez, K. D. Hahn, D. B. Sinars, K. J. Peterson, S. A. Slutz, A. B. Sefkow, T. J. Awe *et al.*, *Phys. Rev. Lett.* **113**, 155004 (2014).
- ²⁶M. Geissel, L. E. Ruggles, A. B. Sefkow, I. C. Smith, J. E. Shores, C. S. Speas, and J. L. Porter, in Proceedings of 41st EPS Conference on Plasma Physics, Berlin, Germany, 26 June 2014.
- ²⁷A. J. Harvey-Thompson, A. B. Sefkow, T. N. Nagayama, M. S. Wei, E. M. Campbell, G. Fiksel, P. Y. Chang, J. R. Davies, D. H. Barnak, V. Y. Glebov *et al.*, *Phys. Plasmas* **22**, 122708 (2015).
- ²⁸A. J. Harvey-Thompson, A. B. Sefkow, M. S. Wei, T. N. Nagayama, E. M. Campbell, B. E. Blue, R. F. Heeter, J. M. Koning, K. J. Peterson, and A. Schmitt, *Phys. Rev. E* **94**, 051201(R) (2016).
- ²⁹M. Geissel, A. J. Harvey-Thompson, T. J. Awe, D. E. Bliss, M. E. Glinsky, M. R. Gomez, E. C. Harding, S. B. Hansen, C. Jennings, M. W. Kimmel *et al.*, *Phys. Plasmas* **25**, 022706 (2018).
- ³⁰S. A. Slutz, W. A. Stygar, M. R. Gomez, K. J. Peterson, A. B. Sefkow, D. B. Sinars, R. A. Vesey, E. M. Campbell, and R. Betti, *Phys. Plasmas* **23**, 022702 (2016).
- ³¹W. A. Stygar, T. J. Awe, J. E. Bailey, N. L. Bennett, E. W. Breden, E. M. Campbell, R. E. Clark, R. A. Cooper, M. E. Cuneo, J. B. Ennis *et al.*, *Phys. Rev. Spec. Top.—Accel. Beams* **18**, 110401 (2015).
- ³²G. B. Zimmerman and W. B. Kruer, *Comments Plasma Phys. Controlled Fusion* **2**, 85 (1975).
- ³³R. D. McBride, C. A. Jennings, R. A. Vesey, G. A. Rochau, M. E. Savage, W. A. Stygar, M. E. Cuneo, D. B. Sinars, M. Jones, K. R. LeChien *et al.*, *Phys. Rev. Spec. Top.—Accel. Beams* **13**, 120401 (2010).
- ³⁴M. R. Gomez, R. M. Gilgenbach, M. E. Cuneo, C. A. Jennings, R. D. McBride, E. M. Waisman, B. T. Hutsel, W. A. Stygar, D. V. Rose, and Y. Maron, *Phys. Rev. Accel. Beams* **20**, 010401 (2017).
- ³⁵B. T. Hutsel, P. A. Corcoran, M. E. Cuneo, M. R. Gomez, M. H. Hess, D. D. Hinshelwood, C. A. Jennings, G. R. Laity, D. C. Lamppa, R. D. McBride *et al.*, *Phys. Rev. Accel. Beams* **21**, 030401 (2018).
- ³⁶G. A. Rochau, J. E. Bailey, R. E. Falcon, G. P. Losel, T. Nagayama, R. C. Mancini, I. Hall, D. E. Winget, M. H. Montgomery, and D. A. Liedahl, *Phys. Plasmas* **21**, 056308 (2014).
- ³⁷M. R. Weis, private communication (2018).
- ³⁸A. J. Harvey-Thompson, M. R. Weis, E. C. Harding, M. Geissel, D. J. Ampleford, G. A. Chandler, J. R. Fein, M. E. Glinsky, M. R. Gomez, and K. D. Hahn, "Diagnosing and mitigating laser preheat induced mix in MagLIF" *Phys. Plasmas* (to be published).
- ³⁹S. B. Hansen, M. R. Gomez, A. B. Sefkow, S. A. Slutz, D. B. Sinars, K. D. Hahn, E. C. Harding, P. F. Knapp, P. F. Schmit, T. J. Awe *et al.*, *Phys. Plasmas* **22**, 056313 (2015).
- ⁴⁰H. A. Scott and S. B. Hansen, *High Energy Density Phys.* **6**, 39 (2010).
- ⁴¹S. B. Hansen, J. Bauche, C. Bauche-Arnoult, and M. F. Gu, "Hybrid atomic models for spectroscopic plasma diagnostics," *High Energy Density Phys.* **3**, 109 (2007).
- ⁴²Y. B. Zel'dovich and Y. P. Raizer, *Physics of Shock Waves and High-Temperature Hydrodynamic Phenomena* (Academic, New York, 1966).
- ⁴³G. Dimonte, *Phys. Plasmas* **7**(6), 2255 (2000).
- ⁴⁴J. K. Hoffer and L. R. Foreman, *Phys. Rev. Lett.* **60**(13), 1310 (1988).
- ⁴⁵A. J. Martin, R. J. Simms, and S. B. Wineberg, *J. Vac. Sci. Technol., A* **7**(3), 1157 (1989).
- ⁴⁶S. A. Slutz, C. A. Jennings, T. J. Awe, G. A. Shipley, B. T. Hutsel, and D. C. Lamppa, *Phys. Plasmas* **24**, 012704 (2017).
- ⁴⁷G. A. Shipley, T. J. Awe, B. T. Hutsel, S. A. Slutz, D. C. Lamppa, J. B. Greenly, and T. M. Hutchinson, *Phys. Plasmas* **25**, 052703 (2018).
- ⁴⁸M. E. Glinsky, private communication (2018).
- ⁴⁹R. Betti, P. Y. Chang, B. K. Spears, K. S. Anderson, J. Edwards, M. Fatenejad, J. D. Lindl, R. L. McCrory, R. Nora, and D. Shvarts, *Phys. Plasmas* **17**, 058102 (2010).
- ⁵⁰R. Betti, A. R. Christopherson, B. K. Spears, R. Nora, A. Bose, J. Howard, K. M. Woo, M. J. Edwards, and J. Sanz, *Phys. Rev. Lett.* **114**, 255003 (2015).
- ⁵¹D. C. Rovang, D. C. Lamppa, M. E. Cuneo, A. C. Owen, J. McKenney, D. W. Johnson, S. Radovich, R. J. Kaye, R. D. McBride, C. S. Alexander *et al.*, *Rev. Sci. Instrum.* **85**, 124701 (2014).
- ⁵²M. C. Jones, D. J. Ampleford, M. E. Cuneo, R. Hohlfelder, C. A. Jennings, D. W. Johnson, B. Jones, M. R. Lopez, J. McArthur, J. A. Mills *et al.*, *Rev. Sci. Instrum.* **85**, 083501 (2014).
- ⁵³E. C. Harding, M. S. Schollmeier, M. R. Gomez, P. F. Knapp, S. B. Hansen, G. K. Robertson, C. S. Speas, D. B. Sinars, G. A. Rochau, J. A. Koch *et al.*, "Single and Dual-Crystal X-ray Microscopes for Large Field-of-View, Self-Emission Imaging on the Z-machine," *Rev. Sci. Instrum.* (submitted).